Supplementary Information

A Multifaceted Ferrocene Interlayer for Highly Stable and Efficient Lithium Doped Spiro-OMeTAD Perovskite Solar Cells

Thomas Webb,* Xueping Liu, Robert J.E. Westbrook, Stefanie Kern, Muhammad T.Sajjad, Sandra Jenatsch, K.D.G. Imalka Jayawardena, W. Hashini K. Perera, Igor Marko, Sanjayan Sathasivam, Bowei Li, Mozhgan Yavari, David J. Scurr, Morgan R. Alexander, Thomas J. Macdonald, Saif A. Haque,* Stephen J. Sweeney,* Wei Zhang*

* Corresponding author. Email: thomas.webb@surrey.ac.uk; s.a.haque@imperial.ac.uk s.sweeney@surrey.ac.uk; wz0003@surrey.ac.uk;

Table S1. Comparison of highest efficiency LiTFSI-doped spiro-OMeTAD devices and leading approaches to replace LiTFSI, highlighting the difference in performance. For a more detailed and comprehensive discussion on stability and alternative dopants for spiro-OMeTAD readers are directed to the work of Ren et al. and Hawash et al.[1,2]

Device architecture	Efficiency (certified)	HTL	Reference
Leading LiTFSI doped Spiro-OMeTAD-based PSCs			
FTO/SnO_2/$FA_xMA_{1-x}PbI_yBr_{3-y}$/Spiro-OMeTAD/Au	25.4 % (25.2 %)	Spiro-OMeTAD + FK209 + tBP+ LiTFSI	[3]
FTO/TiO_2/$FAPbI_3$/Spiro-OMeTAD/Au	25.6 % (25.2 %)	Spiro-OMeTAD + FK209 + tBP + LiTFSI	[4]
FTO/SnO2/$FAPbI_2$:0.38$MDACl_2$/Spiro-OMeTAD/Au	25.8 % (25.5 %)	Spiro-OMeTAD + FK209 + tBP + LiTFSI	[5]
ITO/SnO_2/$FA_xMA_{1-x}PbI_3$/Spiro-OMeTAD/Au	23.5 % (23.3 %)	Spiro-OMeTAD + FK209 + tBP + LiTFSI	[6]
FTO/SnO_2/$FA_xMA_{1-x}PbI_yBr_{3-y}$/Fc/Spiro-OMeTAD/Au	23.4 %	Spiro-OMeTAD + FK209 + tBP + LiTFSI	This work
Leading Alternative Dopants			
FTO/SnO_2/$FA_xMA_{1-x}PbI_yBr_{3-y}$/Spiro-OMeTAD	19.6 %	Spiro-OMeTAD + FK209	[7]
FTO/TiO_2/$FA_xMA_{1-x}PbI_yBr_{3-y}$/Spiro-OMeTAD/Au	22.0 %	Spiro-OMeTAD + tBP + **Zn**$TFSI_2$	[8]
FTO/TiO_2/$FA_xMA_{1-x}PbI_yBr_{3-y}$/Spiro-OMeTAD/Au	20.5 %	Spiro-OMeTAD + tBP + **Ca**$TFSI_2$	[8]
FTO/TiO_2/$FA_xMA_{1-x}PbI_yBr_{3-y}$/Spiro-OMeTAD/Au	20.2 %	Spiro-OMeTAD + tBP + **Cu**$TFSI_2$	[8]
FTO/TiO_2/$FA_xMA_{1-x}PbI_yBr_{3-y}$/Spiro-OMeTAD/Au	20.4 %	Spiro-OMeTAD + tBP + **Sc**$TFSI_2$	[8]
FTO/TiO_2/$FA_xMA_{1-x}PbI_yBr_{3-y}$/Spiro-OMeTAD/Au	18.6 %	Spiro-OMeTAD + tBP + **Mg**$TFSI_2$	[9]
FTO/TiO_2/$FA_xMA_{1-x}PbI_yBr_{3-y}$/Spiro-OMeTAD/Au	21.1 %	Spiro-OMeTAD + tBP + **Na**TFSI	[10]
ITO/SnO_2/$FA_xMA_{1-x}PbI_yBr_{3-y}$/Spiro-OMeTAD/Au	18.6 %	Spiro-OMeTAD + tBP + (**MeO-TPD**)TFSI	[11]
ITO/SnO_2/$FA_xMA_{1-x}PbI_yBr_{3-y}$/Spiro-OMeTAD/Au	17.8 %	Spiro-OMeTAD + tBP + **Spiro**$TFSI_2$	[11]
FTO/TiO_2/$FA_xMA_{1-x}PbI_yBr_{3-y}$/Spiro-OMeTAD/Au	14.0 %	Spiro-OMeTAD + tBP + **BMPy**TFSI	[12]
FTO/TiO_2/$FA_xMA_{1-x}PbI_yBr_{3-y}$/Spiro-OMeTAD/Au	20.3 %	Spiro-OMeTAD + tBP + **PVBI**TFSI	[13]
Leading Alternative HTLs to Spiro-OMeTAD			
FTO/TiO_2/$FA_xMA_{1-x}PbI_yBr_{3-y}$/PTAA/Au	22.2 %	PTAA	[14]
FTO/TiO_2/$FA_xMA_{1-x}PbI_yBr_{3-y}$/P3HT/Au	22.8 % (22.7 %)	P3HT	[15]
FTO/TiO_2/$CsFA_xMA_{1-x}PbI_yBr_{3-y}$/CuSCN/Au	20.4 %	CuSCN	[16]
ITO/SnO_2/$FA_xMA_{1-x}PbI_yBr_{3-y}$/PBTFO/Au	22.1 %	PBTFO	[17]
FTO/TiO_2/$Cs_xFA_{1-x}PbI_3$/YZ22/Au	22.4 %	YZ22	[18]

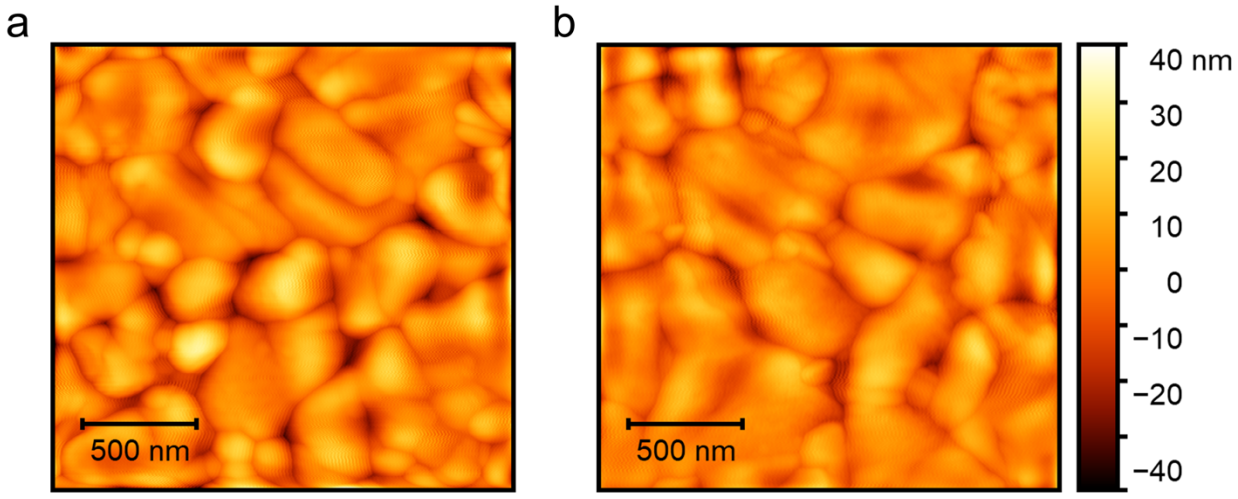

Figure S1: AFM images of control and ferrocene modified perovskite films. a) control perovskite film. b) perovskite film modified with ferrocene.

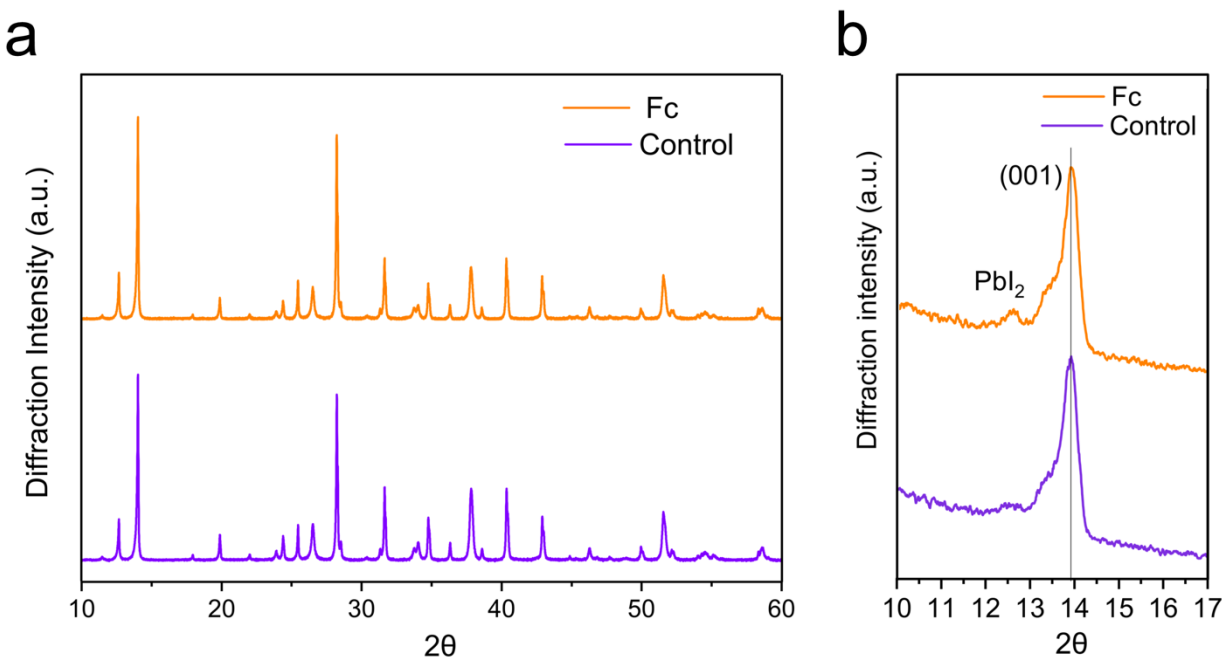

Figure S2: Diffraction patterns of ferrocene modified perovskite films. a) X-ray diffraction pattern of perovskite films in a pseudo-powder Bragg-Brentano geometry. b) Surface sensitive Grazing Incidence X-ray diffraction, incident angle (ω) set to 0.5 °, [001] peak of the 3D phase highlighted. No significant changes in the [001] are observed indicating no distortion of the perovskite at the interface following ferrocene deposition.

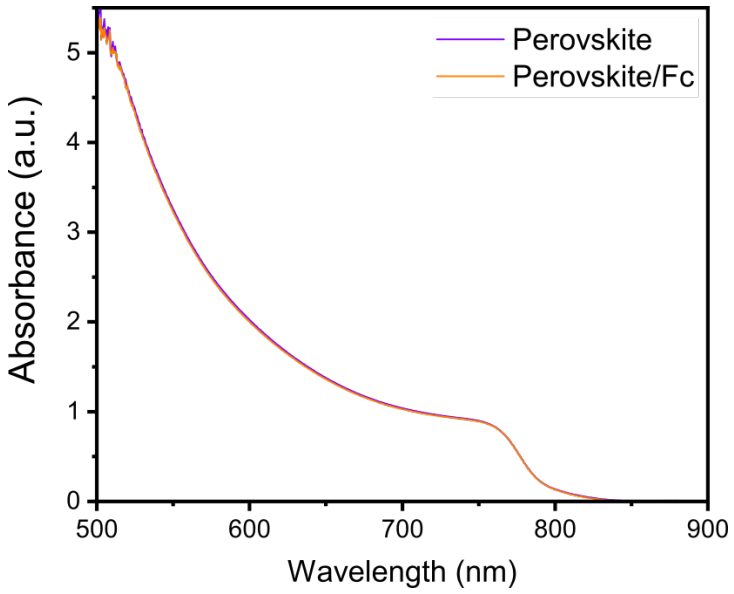

Figure S3: UV-visible absorbance spectra of perovskite films with and without a ferrocene modification revealing negligible changes in the absorbance profile and optical band gap.

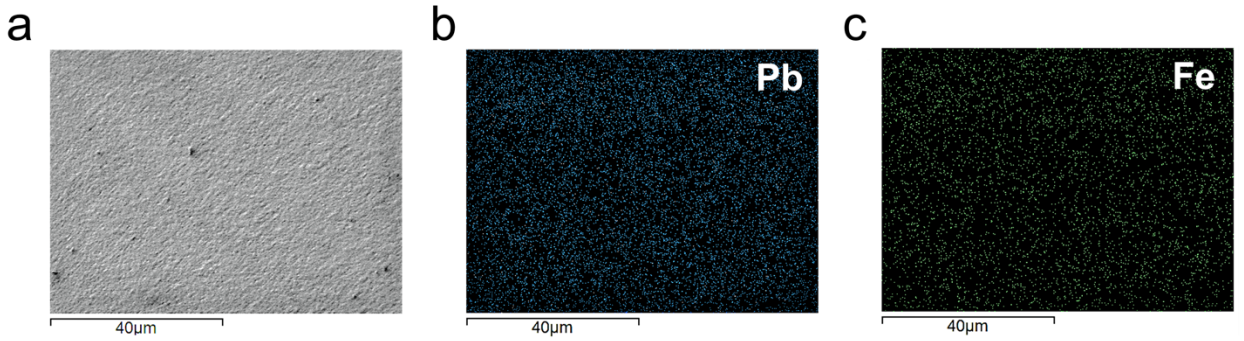

Figure S4: Energy Dispersive X-ray (EDX) spectroscopy. a) SEM image of area of interest on the ferrocene modified perovskite thin films. b) EDX map of Pb counts. c) EDX map of Fe counts attributed to ferrocene, showing a uniform dispersion across the film.

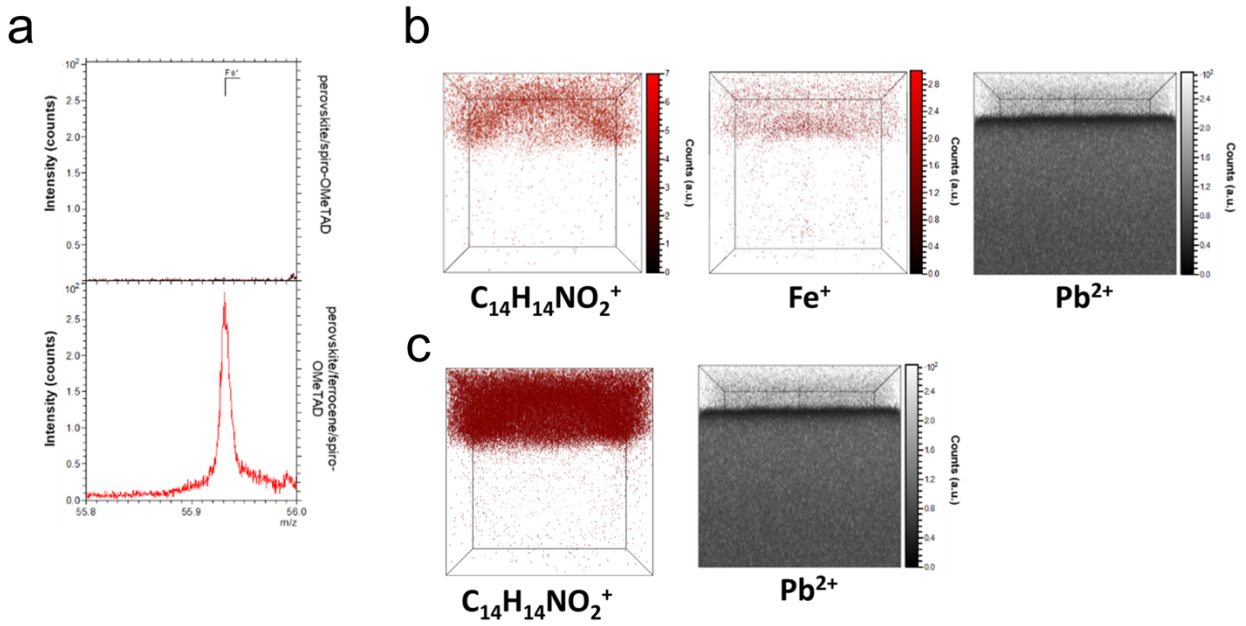

Figure S5: OrbiSIMS data, a) Spectra overlay of Fe^+ in perovskite/spiro-OMeTAD (top) and perovskite/ferrocene/spiro-OMeTAD (below). We therefore conclude that Fe, attributed to ferrocene, is only present in ferrocene treated devices. b) 3D reconstructed secondary ion images of $C_{14}H_{14}NO_2^+$ (spiro-OMeTAD), Fe^+ (Ferrocene) and Pb^{2+} (perovskite). The 3D images reveal a high concentration of ferrocene located at the interface and diffusion into the Spiro-OMeTAD layer. c) $C_{14}H_{14}NO_2^+$ (spiro-OMeTAD) distribution in films prepared without ferrocene, changes in absolute intensity are attributed to matrix.

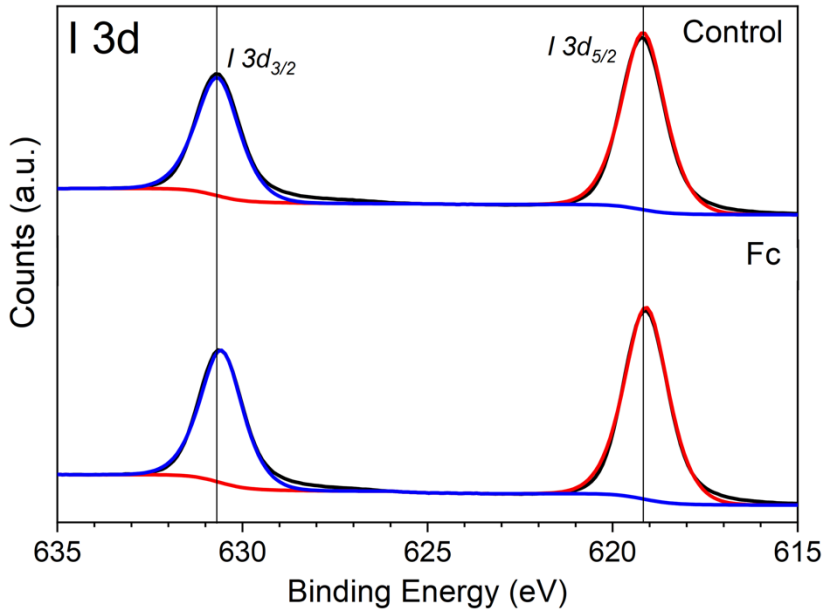

Figure S6: XPS spectra of I 3d orbitals. Addition of ferrocene (bottom) leads to negligible changes in peak position.

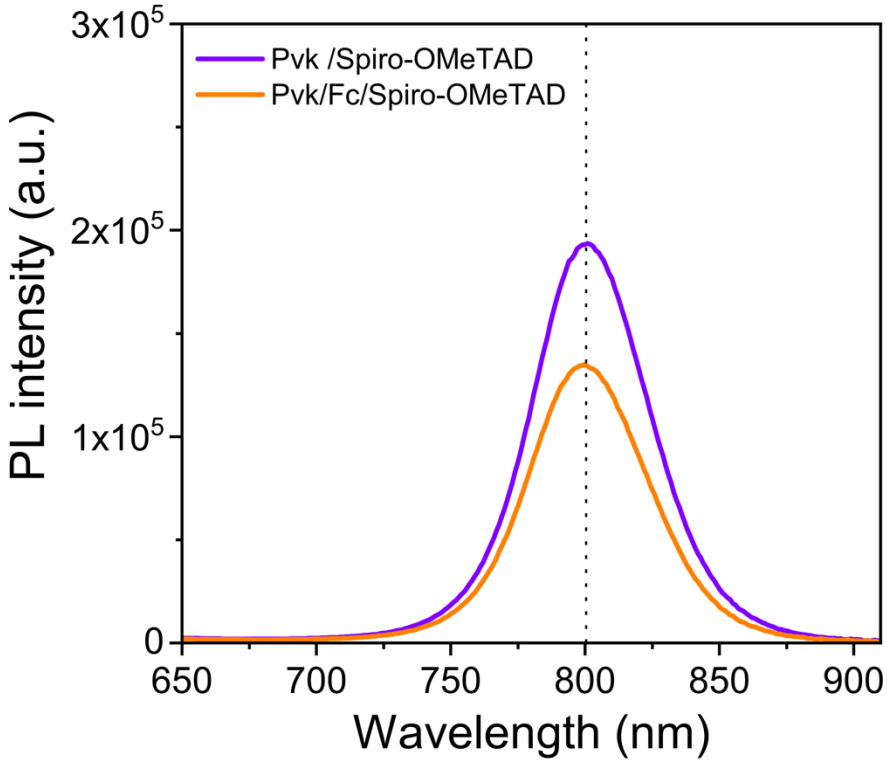

Figure S7: Magnified steady-state PL emission of perovskite/spiro-OMeTAD films prepared with and without ferrocene. Increased quenching in the ferrocene modified film (orange) is attributed to improved hole extraction, reducing the number of electron-hole pairs within the perovskite that can recombine radiatively.

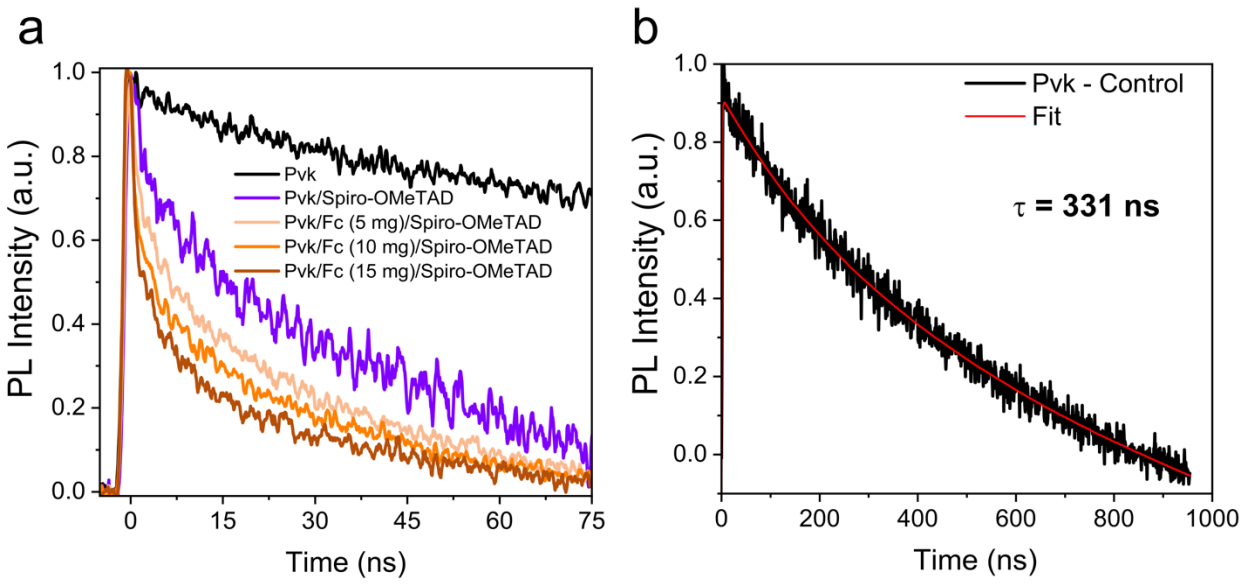

Figure S8: Supplementary transient PL spectroscopy data, a) TRPL data of perovskite films modified with difference concentrations of ferrocene. The TRPL reveals decreasing radiative lifetimes with increasing ferrocene concentration at the interface attributed to faster hole extraction kinetics in samples prepared with increasing ferrocene. b) Transient PL decay and decay fit of the control unquenched perovskite film measured up to 1 μs.

Table S2. Tabulated TRPL lifetimes and quenching efficiencies of perovskite films modified with difference concentrations of ferrocence

Samples	τ_1**(ns)**	τ_2**(ns)**	τ_{avgInt}**(ns)**	ϕ **(%)**
PVK/control	331 ± 10 (100%)	-	331± 10	-
PVK/Spiro-OMeTAD	2.0 ± 0.2 (3%)	41 ± 4 (97%)	41 ± 4	61 ± 3
PVK/Fc (5 mg)/ Spiro-OMeTAD	2.0 ± 0.2 (6%)	32 ± 3 (94%)	32 ± 3	73 ± 4
PVK/Fc (10 mg)/ Spiro-OMeTAD	1.0 ± 0.1 (8%)	30 ± 3 (92%)	30 ± 3	78 ± 4
PVK/Fc (15 mg)/ Spiro-OMeTAD	1.0 ± 0.1 (12%)	28 ± 3 (88%)	27 ± 3	82 ± 4

Supplementary Note 1.

Calculation of charge quenching efficiency

Lifetimes (τ_1, τ_2) were fitted using $f(t) = A(\%)_1 e^{-\frac{t}{\tau_1}} + A(\%)_2 e^{-\frac{t}{\tau_2}}$

Average lifetime is calculated using

$$\tau_{avg} = \frac{A_1\tau_1^2 + A_2\tau_2^2}{A_1\tau_1 + A_2\tau_1}$$

Where $\boldsymbol{\phi}$ is the charge transfer efficiency calculated using

$$\boldsymbol{\phi} = 1 - \frac{\int I_{PVK\ with\ quencher}}{\int I_{PVK\ control}}$$

Supplementary Note 2,

Previous work by Marchioro et al. and Shen et al. has highlighted that bimolecular recombination between the perovskite conduction band and injected holes in the spiro-OMeTAD is the dominant recombination mechanism of injected holes in spiro-OMeTAD-based DSSC films, in perovskite films of differing composition[19,20]. This can be rationalized by the slow rate of monomolecular recombination of the injected hole population within the HTL. Furthermore, identical recombination pathways between electrons in the absorber conduction band and holes in the spiro-OMeTAD have been identified using alternative absorbers to metal halide perovskite including Sb_2S_3 and Sb_2Se_3[21,22]. These studies combined with those conducted on perovskites demonstrate that the recombination mechanism of bimolecular recombination across the interface is dominant in spiro-OMeTAD compared to monomolecular recombination, assuming similar conduction band energies. Nevertheless, the evidence of bimolecular recombination in previous works has relied heavily on the comparison of ΔOD decay in spiro-OMeTAD films prepared on an absorber prepared on a mp-TiO_2 and mp-Al_2O_3 substrates. In the case of the latter high electron densities in the conduction band, from reduced electron extraction, leads to faster rates of recombination and shorter decays of the oxidized spiro-OMeTAD transient[19,20]. To offer more evidence on this point a simple measurement was conducted using an archetypal $MAPbI_3$ film pumped with increasing carrier densities before recording the change in the recombination rate of the spiro-OMeTAD. From Supplementary Fig. 9 we observe that the rate of recombination in the spiro-OMeTAD increases monotonically with carrier density and supports the conclusion that the recombination pathway is related on the electrons in the conduction band, consistent with the reported interfacial bimolecular recombination pathway.

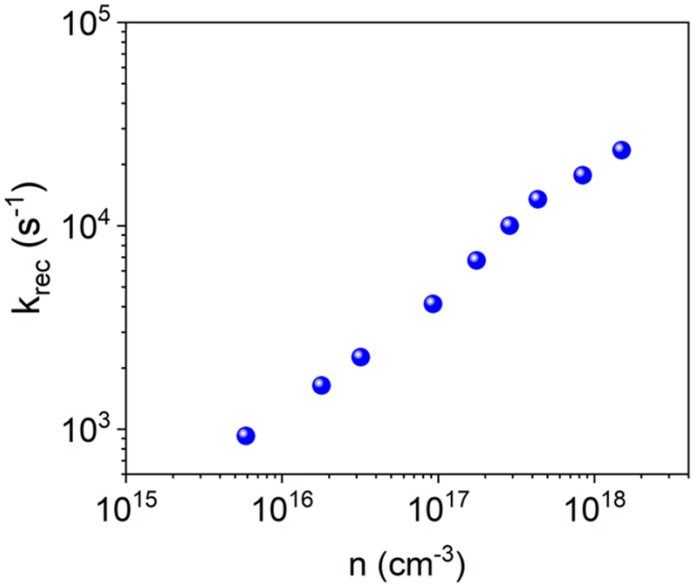

Figure S9: Recombination rate constant, k_{rec}, measured as 1/ τ_{rec} - of spiro-OMeTAD holes plotted against carrier density, *n*. Data showing bimolecular recombination as the dominant recombination mechanism consistent with previously reported in the literature. monotonic relationship between recombination rate of spiro-OMeTAD hole polaron and carrier density in the perovskite conduction band. Samples prepared using an archetypal $MAPbI_3$/spiro-OMeTAD system to investigate the recombination kinetics of spiro-OMeTAD.

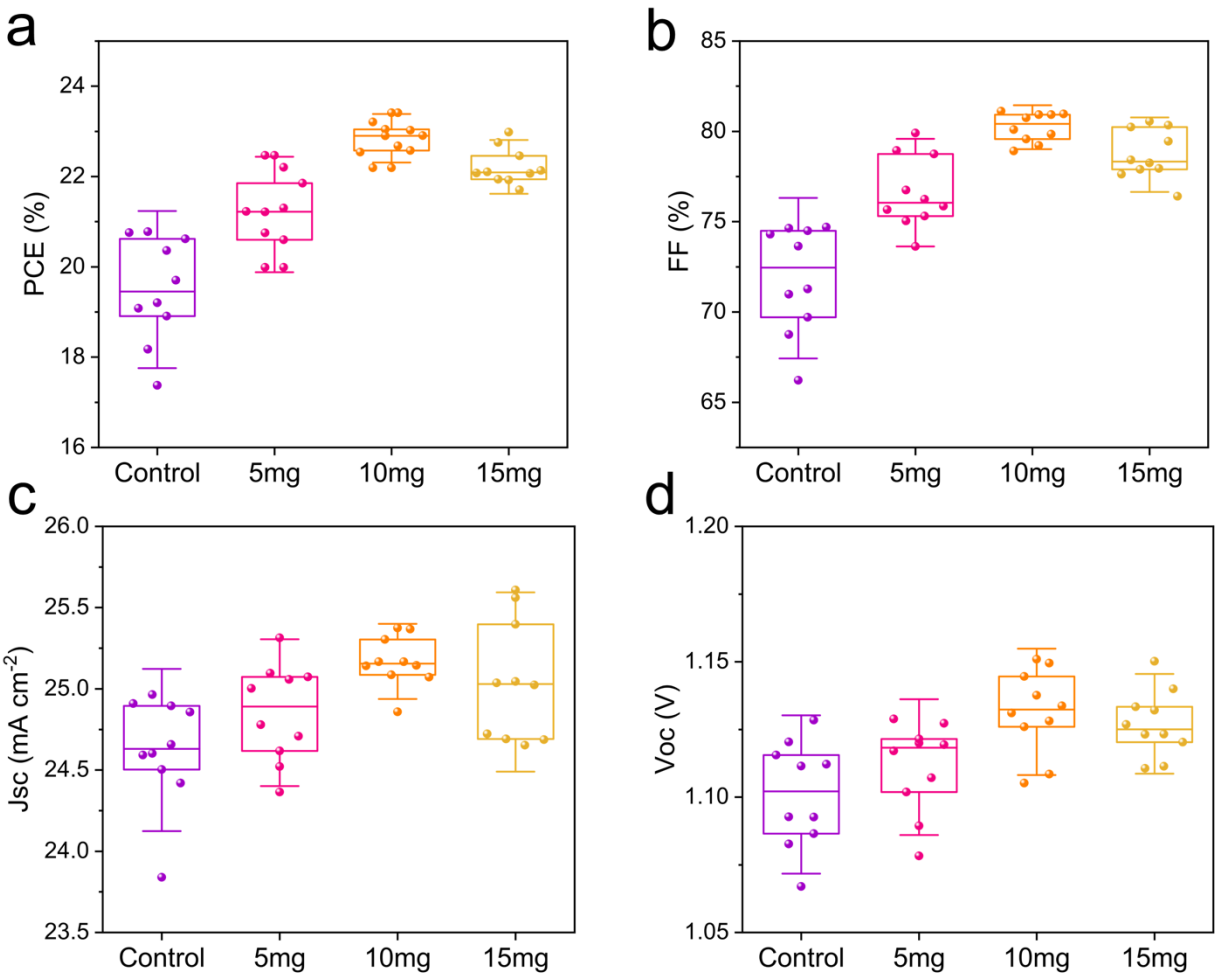

Figure S10: Statistical data for PSCs prepared with varying ferrocene concentration a) is PCE, b) is FF, c) is J_{SC}, and d) is V_{OC}. Consistent with the increasing quenching in TRPL PSC performance increases with increasing ferrocene concentration from 0 to 5 to 10 mg mL^{-1}. Interestingly at 15 mg mL^{-1} a drop in performance is noted. While it is not clear on the origin of this drop, we suggest it could be a consequence of an excessive spiro-$OMeTAD^+$ concentration. Indeed, previous works by study by Sanchez et al. revealed that at Spiro-$OMeTAD^+$ concentrations over 4 mol % the J_{SC} is reduced[23]. Additionally, PSCs prepared with high concentrations of spiro-$OMeTAD^+$ exhibit poor stability and reproducibility. This is also reflected here in the J_{SC} of PSCs prepared with 15 mg mL^{-1} of spiro-OMeTAD.

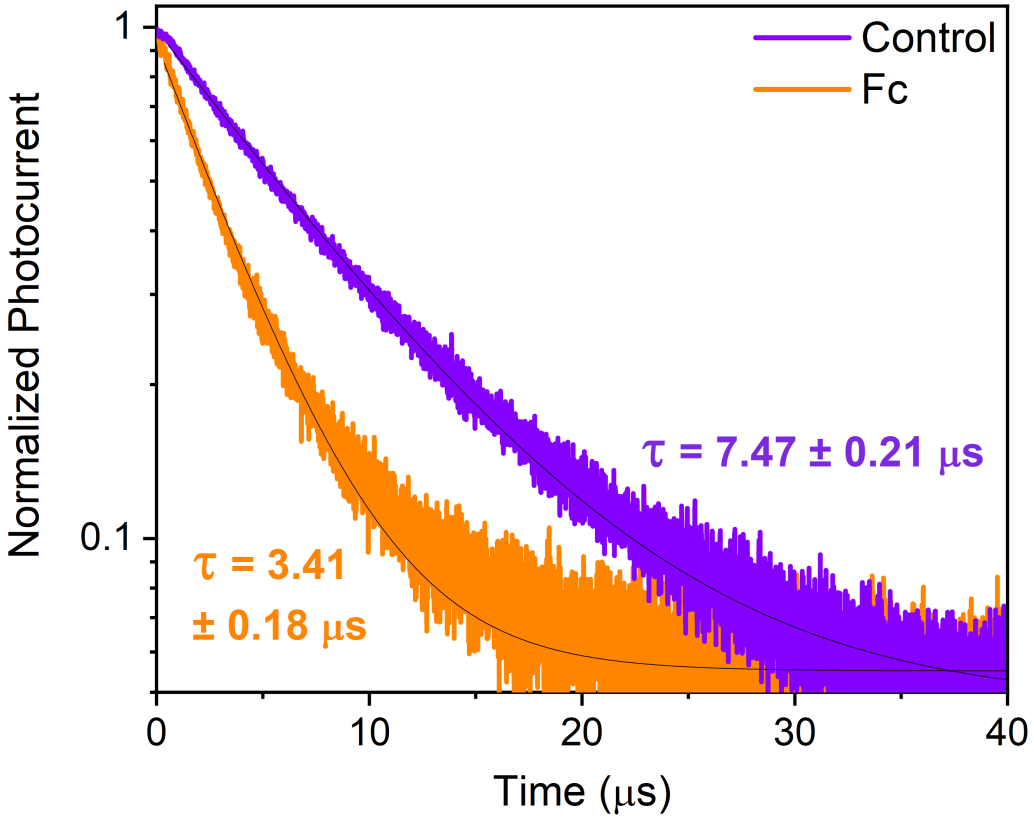

Figure S11: Fitting of transient photocurrents. Fits of the TPC curves for PSCs with and without ferrocene modification. The plot of log photocurrent against time shows a linear decay. A semi-log plot is used here to demonstrate the monoexponential decay of photocurrent out the PSC.

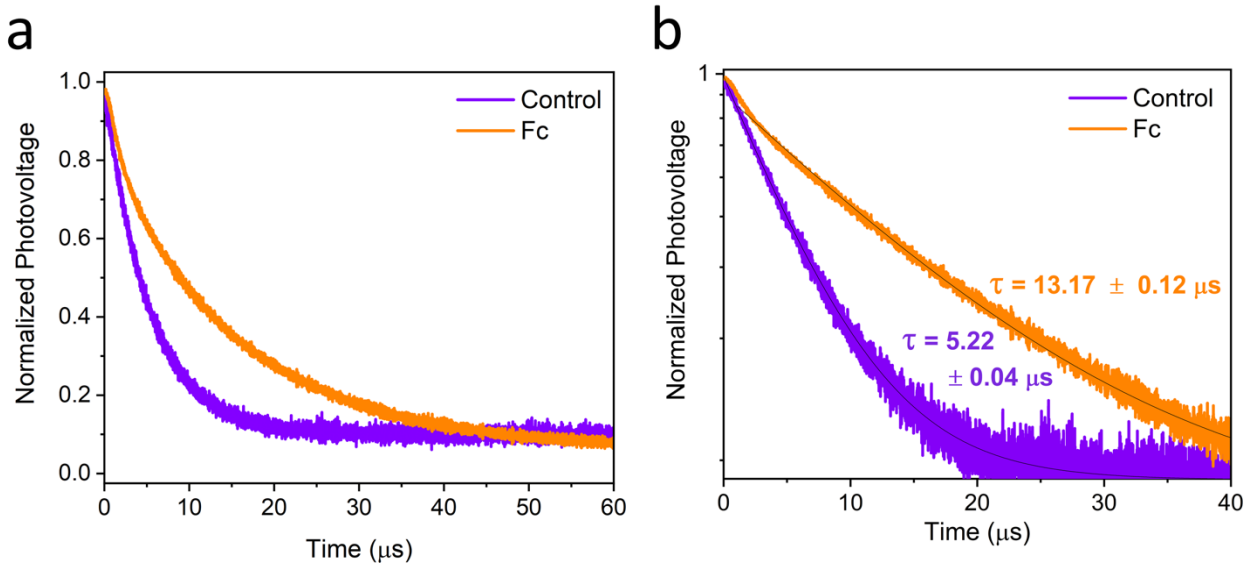

Figure S12: Transient photovoltage decays. a) Photovoltage decays of PSCs with and without ferrocene modification. b) Fitting of transient photovoltage decay curves using a monoexponential fit. A semi-log plot is used here to demonstrate the monoexponential decay of the photovoltage in the operational PSC**.**

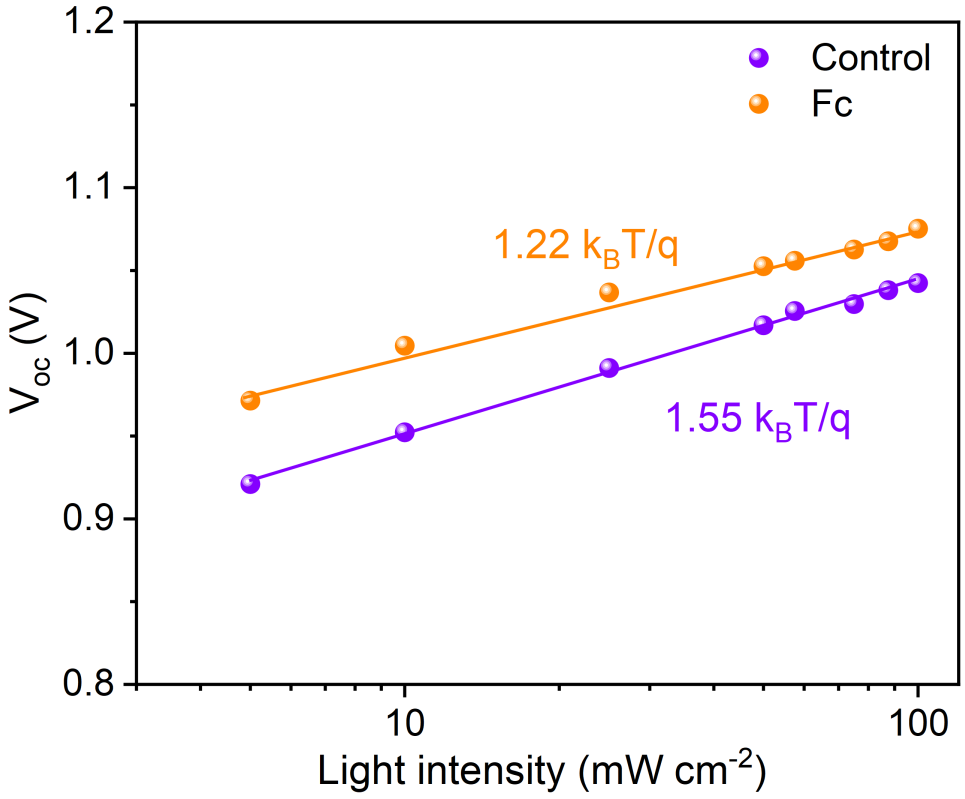

Figure S13: Illumination intensity dependent photovoltage. Dependence of light intensity on V_{OC} of PSCs with and without ferrocene modification. Samples measured via increasing light intensity from 2 mW cm^{-2} (0.02 Suns) to 100 mW cm^{-2} (1 Sun).

Supplementary Note 3.

Preparation of undoped devices

Undoped devices are presented in this paper as preliminary data for the use of ferrocene as a potential alternative to conventional dopants. To make devices prepared with undoped spiro-OMeTAD comparable to other articles in the literature, a simplified $MAPbI_3$ perovskite is utilized. A standard and processing one-step method combining MAI and PbI_2 in a 1:1 molar ratio in DMSO:DMF (1:9, volume ratio).

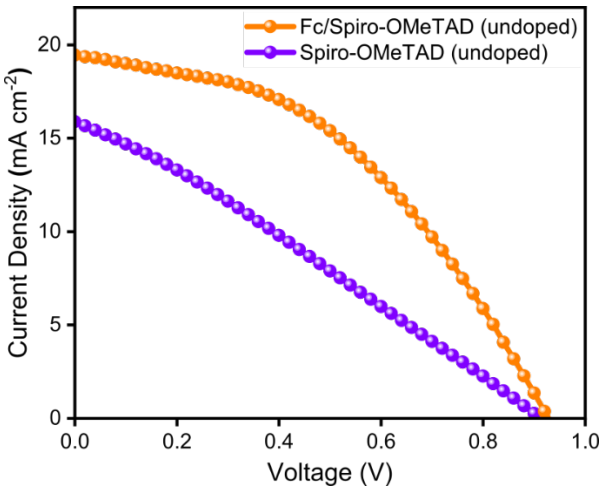

Figure S14: *J-V* curves of champion undoped spiro-OMeTAD PSCs. *J-V* curve data of ITO/SnO_2/$MAPbI_3$/Spiro-OMeTAD/Ag devices prepared without any dopants (LiTFSI, FK209, or tBP) in the spiro-OMeTAD. Device parameters V_{OC}= 0.93, J_{SC} = 19.45 mA cm^{-2}, FF= 0.43, PCE = 7.83 % for ferrocene modified devices. Device parameters V_{OC} = 0.91, J_{SC} = 15.88 mA cm^{-2}, FF = 0.27, PCE= 3.98 % for control devices.

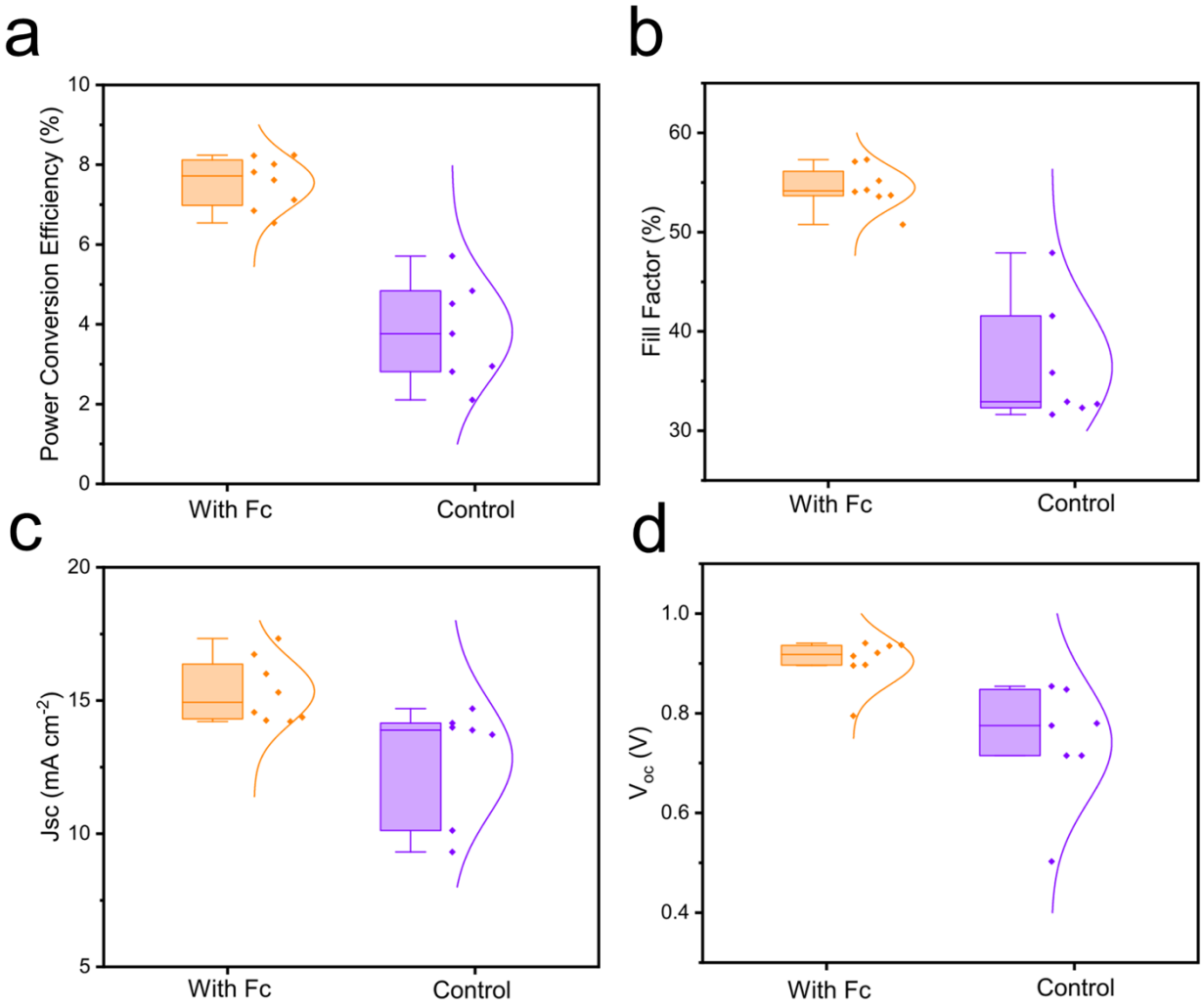

Figure S15: Device statistics of undoped spiro-OMeTAD devices. PSC performance parameters of 7 devices prepared with and without ferrocene using an ITO/SnO_2/$MAPbI_3$/Spiro-OMeTAD/Ag device structure.

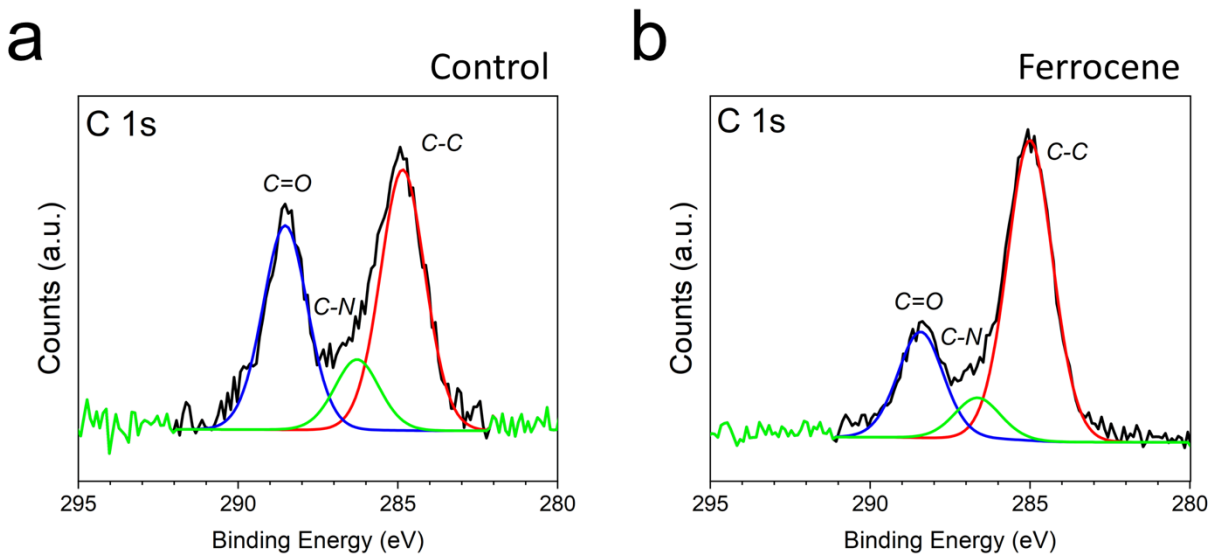

Figure S16: XPS spectra of C 1s orbitals in films prepared without a) and with b) ferrocene.

Supplementary Note 4. We note the C-N interaction of the perovskite is slightly damped in figure b) owing to the addition of a ferrocene contribution to the interface chemistry. In comparison the fraction of C=O interactions at the interface are significantly reduced affording the film greater tolerance to ambient conditions.

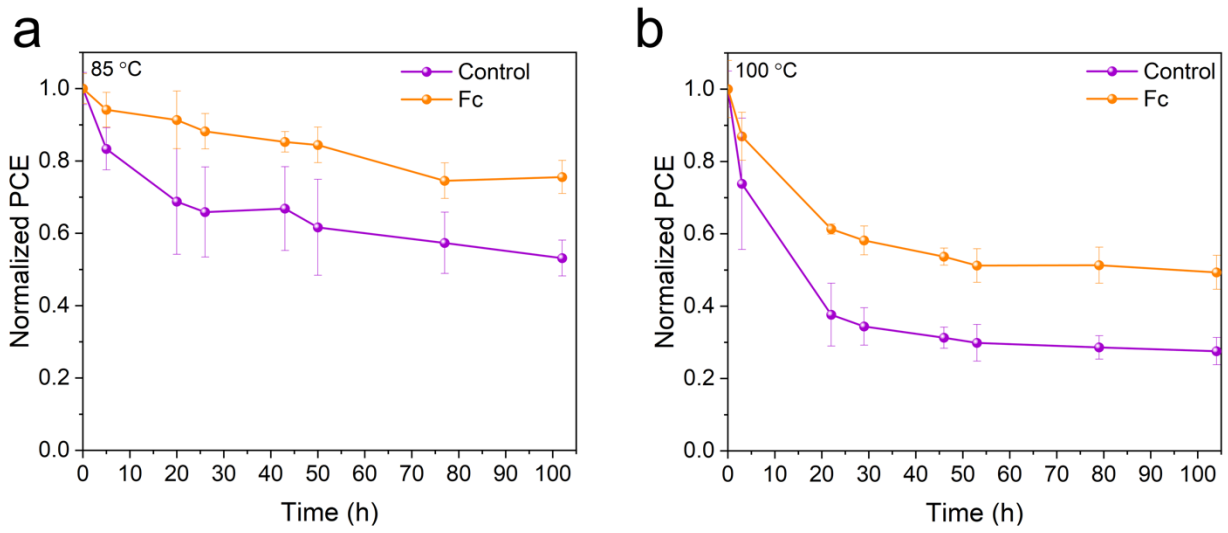

Figure S17: High temperature stability of PSCs prepared with and without ferrocene at a) 85 ºC and b) 100 ºC. Samples stored at chosen temperature within a N_2 filled glovebox.

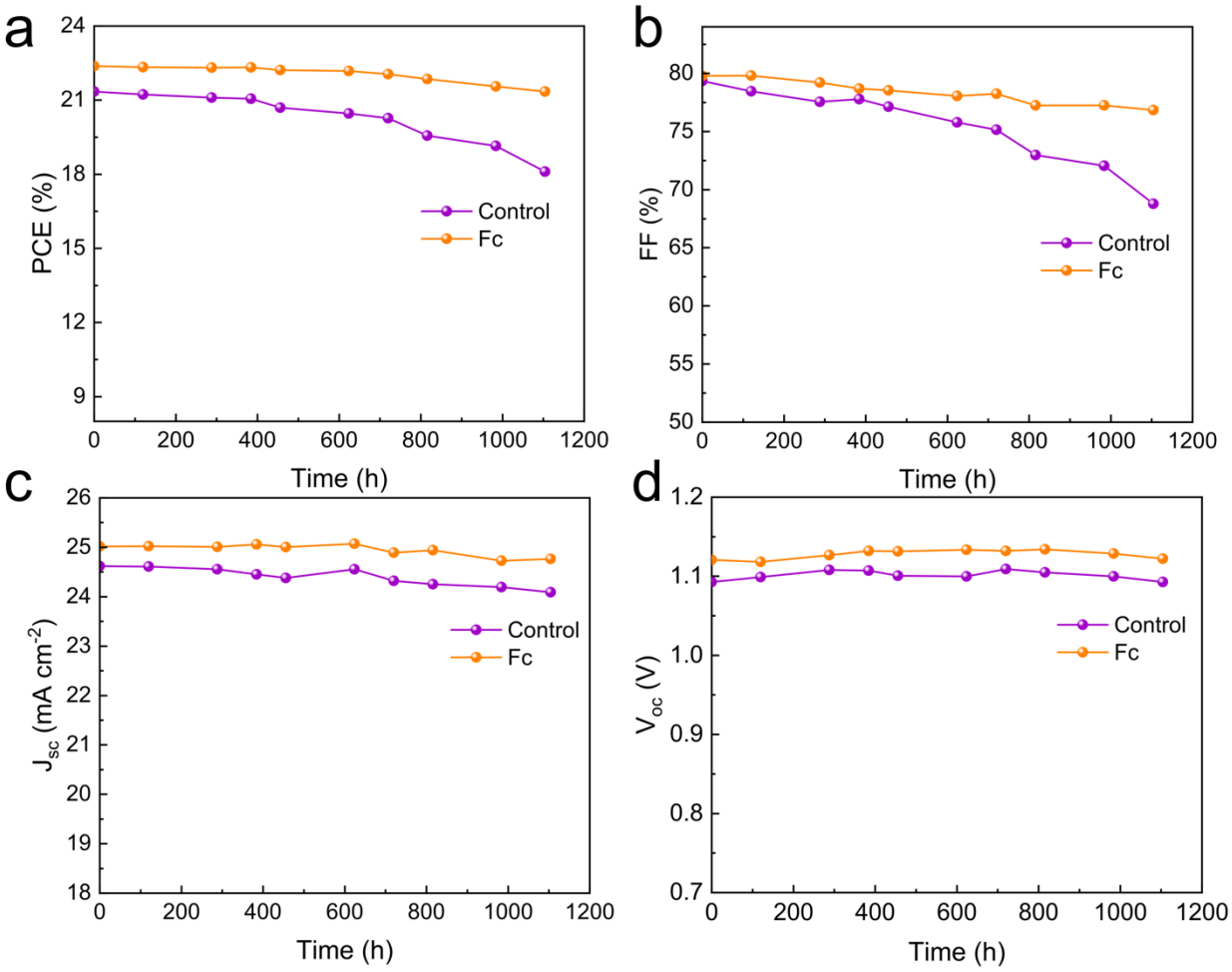

Figure S18: Supplementary ISOS D-1 stability PSC tracking. PSC performance parameters plotted of devices stored under ISOS D-1 conditions (dark storage) in ambient conditions over a duration of 1100 h[24].

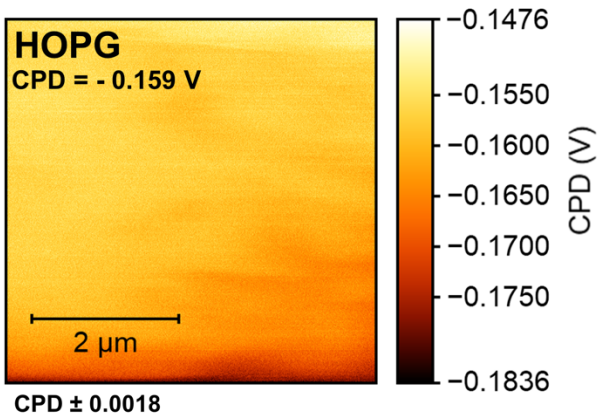

Figure S19: KPFM surface potential of highly oriented pyrolytic graphite (HOPG) following exfoliation.

References

[1] G. Ren, W. Han, Y. Deng, W. Wu, Z. Li, J. Guo, H. Bao, C. Liu, W. Guo, *J. Mater. Chem. A* **2021**, *9*, 4589.

[2] Z. Hawash, L. K. Ono, Y. Qi, *Advanced Materials Interfaces* **2018**, *5*, 1700623.

[3] J. J. Yoo, G. Seo, M. R. Chua, T. G. Park, Y. Lu, F. Rotermund, Y.-K. Kim, C. S. Moon, N. J. Jeon, J.-P. Correa-Baena, V. Bulović, S. S. Shin, M. G. Bawendi, J. Seo, *Nature* **2021**, *590*, 587.

[4] J. Jeong, M. Kim, J. Seo, H. Lu, P. Ahlawat, A. Mishra, Y. Yang, M. A. Hope, F. T. Eickemeyer, M. Kim, Y. J. Yoon, I. W. Choi, B. P. Darwich, S. J. Choi, Y. Jo, J. H. Lee, B. Walker, S. M. Zakeeruddin, L. Emsley, U. Rothlisberger, A. Hagfeldt, D. S. Kim, M. Grätzel, J. Y. Kim, *Nature* **2021**, *592*, 381.

[5] H. Min, D. Y. Lee, J. Kim, G. Kim, K. S. Lee, J. Kim, M. J. Paik, Y. K. Kim, K. S. Kim, M. G. Kim, T. J. Shin, S. Il Seok, *Nature* **2021**, *598*, 444.

[6] Q. Jiang, Y. Zhao, X. Zhang, X. Yang, Y. Chen, Z. Chu, Q. Ye, X. Li, Z. Yin, J. You, *Nat. Photonics* **2019**, *13*, 460.

[7] G. Zhu, L. Yang, C. Zhang, G. Du, N. Fan, Z. Luo, X. Zhang, J. Zhang, *ACS Appl. Energy Mater.* **2022**, *5*, 3595.

[8] J.-Y. Seo, S. Akin, M. Zalibera, M. A. R. Preciado, H.-S. Kim, S. M. Zakeeruddin, J. V. Milić, M. Grätzel, *Advanced Functional Materials* **2021**, *31*, 2102124.

[9] N. D. Pham, J. Shang, Y. Yang, M. T. Hoang, V. T. Tiong, X. Wang, L. Fan, P. Chen, L. Kou, L. Wang, H. Wang, *Nano Energy* **2020**, *69*, 104412.

[10] S.-M. Bang, S. S. Shin, N. J. Jeon, Y. Y. Kim, G. Kim, T.-Y. Yang, J. Seo, *ACS Energy Lett.* **2020**, *5*, 1198.

[11] W. Zhang, F. Zhang, B. Xu, Y. Li, L. Wang, B. Zhang, Y. Guo, J. M. Gardner, L. Sun, L. Kloo, *ACS Appl. Mater. Interfaces* **2020**, *12*, 33751.

[12] J. Zhang, T. Zhang, L. Jiang, U. Bach, Y.-B. Cheng, *ACS Energy Lett.* **2018**, *3*, 1677.

[13] C. Geffroy, E. Grana, T. Bessho, S. Almosni, Z. Tang, A. Sharma, T. Kinoshita, F. Awai, E. Cloutet, T. Toupance, H. Segawa, G. Hadziioannou, *ACS Appl. Energy Mater.* **2020**, *3*, 1393.

[14] W. S. Yang, B.-W. Park, E. H. Jung, N. J. Jeon, Y. C. Kim, D. U. Lee, S. S. Shin, J. Seo, E. K. Kim, J. H. Noh, S. I. Seok, *Science* **2017**, *356*, 1376.

[15] E. H. Jung, N. J. Jeon, E. Y. Park, C. S. Moon, T. J. Shin, T.-Y. Yang, J. H. Noh, J. Seo, *Nature* **2019**, *567*, 511.

[16] Neha Arora, M. Ibrahim Dar, Alexander Hinderhofer, Norman Pellet, Frank Schreiber, Shaik Mohammed Zakeeruddin, Michael Gratzel, *Science* **2017**, *358*, 768.

[17] Z. Li, J. Park, H. Park, J. Lee, Y. Kang, T. K. Ahn, B.-G. Kim, H. J. Park, *Nano Energy* **2020**, *78*, 105159.

[18] B. X. Zhao, C. Yao, K. Gu, T. Liu, Y. Xia, Y.-L. Loo, *Energy Environ. Sci.* **2020**, *13*, 4334.

[19] A. Marchioro, J. Teuscher, D. Friedrich, M. Kunst, R. van de Krol, T. Moehl, M. Grätzel, J.-E. Moser, *Nature Photon* **2014**, *8*, 250.

[20] Q. Shen, Y. Ogomi, J. Chang, S. Tsukamoto, K. Kukihara, T. Oshima, N. Osada, K. Yoshino, K. Katayama, T. Toyoda, S. Hayase, *Physical Chemistry Chemical Physics* **2014**, *16*, 19984.

[21] F. T. F. O'Mahony, T. Lutz, N. Guijarro, R. Gómez, S. A. Haque, *Energy & Environmental Science* **2012**, *5*, 9760.
[22] N. Guijarro, T. Lutz, T. Lana-Villarreal, F. O'Mahony, R. Gómez, S. A. Haque, *J. Phys. Chem. Lett.* **2012**, *3*, 1351.
[23] R. S. Sanchez, E. Mas-Marza, *Solar Energy Materials and Solar Cells* **2016**, *158*, 189.
[24] M. V. Khenkin, E. A. Katz, A. Abate, G. Bardizza, J. J. Berry, C. Brabec, F. Brunetti, V. Bulović, Q. Burlingame, A. Di Carlo, R. Cheacharoen, Y.-B. Cheng, A. Colsmann, S. Cros, K. Domanski, M. Dusza, C. J. Fell, S. R. Forrest, Y. Galagan, D. Di Girolamo, M. Grätzel, A. Hagfeldt, E. von Hauff, H. Hoppe, J. Kettle, H. Köbler, M. S. Leite, S. (Frank) Liu, Y.-L. Loo, J. M. Luther, C.-Q. Ma, M. Madsen, M. Manceau, M. Matheron, M. McGehee, R. Meitzner, M. K. Nazeeruddin, A. F. Nogueira, Ç. Odabaşı, A. Osherov, N.-G. Park, M. O. Reese, F. De Rossi, M. Saliba, U. S. Schubert, H. J. Snaith, S. D. Stranks, W. Tress, P. A. Troshin, V. Turkovic, S. Veenstra, I. Visoly-Fisher, A. Walsh, T. Watson, H. Xie, R. Yıldırım, S. M. Zakeeruddin, K. Zhu, M. Lira-Cantu, *Nat Energy* **2020**, *5*, 35.